

Article

Large-Eddy Simulations of Unsteady Reaction Flow Characteristics Using Four Geometrical Combustor Models

Nan Meng and Feng Li * 

School of Energy and Power Engineering, Beihang University, Beijing 100191, China

* Correspondence: lifeng1966buaa@126.com

Abstract: Combustion instability constitutes the primary loss source of combustion chambers, gas turbines, and aero engines, and it affects combustion performance or results in a sudden local oscillation. Therefore, this study investigated the factors affecting flame fluctuation on unsteady combustion flow fields through large-eddy simulations. The effects of primary and secondary holes in a triple swirler staged combustor on flame propagation and pressure fluctuation in a combustion field were studied. Moreover, the energy oscillations and dominant frequencies in the combustion field were obtained using the power spectral density technique. The results revealed a variation in the vortex structure and Kelvin–Helmholtz instability in the combustion field, along with a variation in the pressure pulsation during flame propagation under the influence of the primary and secondary hole structures. Additionally, the spatial distributions of pressure oscillation and heat release rate amplitude were obtained, revealing that the foregoing increased owing to the primary and secondary holes in the combustion field, reaching a peak in the shear layer and vortex structure regions.

Keywords: combustion instability; triple swirler combustor; large-eddy simulation; pressure fluctuation; flame dynamics



Citation: Meng, N.; Li, F. Large-Eddy Simulations of Unsteady Reaction Flow Characteristics Using Four Geometrical Combustor Models.

Aerospace **2023**, *10*, 147. <https://doi.org/10.3390/aerospace10020147>

Academic Editor: Sergey Leonov

Received: 16 December 2022

Revised: 31 January 2023

Accepted: 2 February 2023

Published: 6 February 2023



Copyright: © 2023 by the authors. Licensee MDPI, Basel, Switzerland. This article is an open access article distributed under the terms and conditions of the Creative Commons Attribution (CC BY) license (<https://creativecommons.org/licenses/by/4.0/>).

1. Introduction

Combustion instability represents the primary loss source of combustion chambers [1], gas turbines [2], and aero engines [3]. It is primarily manifested through large-scale fluctuations that can severely affect combustion performance, potentially causing a sudden increase in local heat release [4]. This can, in turn, trigger large-scale flame fluctuations, affecting combustion performance or resulting in a sudden local thermoacoustic oscillation [5,6]. Therefore, it is essential to mitigate aero-engine instability [7].

Recently, the focus of research on combustion instability has evolved from simple laminar flame burners [8] to complex turbulent flame burners [9]. Most previous studies have focused on controlling the equivalence ratio and boundary conditions [10,11]. In particular, Ren et al. [12] explored pressure fluctuations and the driving mechanisms of various equivalence ratios and combustion modes through numerical simulations. Palies et al. [13] studied the dynamics of premixed flames based on incident velocity and concluded that an unsteady heat release is triggered by the combined action of axial and azimuthal velocities. Ozgunoglu et al. [14] elucidated the interaction between complex turbulent flow fields and flame dynamics in a non-premixed combustor. Huang et al. [15] analyzed turbulent combustion characteristics under various combustion pressures and equivalent ratios using the large-eddy simulation (LES) of a combustion chamber. Guo et al. [16] used numerical simulations to explore longitudinal combustion instabilities, including the coupling among acoustics, fluid mechanics, and heat release. Zeng et al. [17] conducted a numerical simulation of an unsteady turbulent flow field by comparing combustion chamber models with and without blunt bodies. In general, these studies have demonstrated that combustion instability is usually sensitive to the geometry and boundary conditions of the combustion chamber.

Several scholars have studied the pressure spectrum and hydrodynamic characteristics of dynamic combustion in an aero-engine combustion chamber. Wu et al. [18] studied the effect of outlet geometry contraction on the precessing vortex core (PVC) and the vortex breakdown structure in a combustor. Stöhr et al. [19] elucidated the coupling of a helical PVC in a combustion chamber and flame development in a turbulent flow field. Salvador et al. [20] analyzed the low-order coherent structure of a high-swirl combustor. They also conducted a numerical study of the unreacted flow field through proper orthogonal and dynamic mode decomposition techniques. Zhang et al. [21] applied a self-developed high-order numerical solver to examine the effect of hydrodynamic characteristics on thermoacoustic instability in a swirl-stabilized combustion chamber. Nam and Yoh [22] elucidated the driving source of combustion instability by analyzing the pressure spectrum and harmonic modes of unsteady flames. Song et al. [23] investigated the characteristics of longitudinal combustion instability using an analytical model of flame motion in a combustor. However, the dynamic combustion characteristics of a complex multistage swirler, particularly the combustion instability of the primary and secondary holes in a triple-swirl combustion chamber, have not been studied in detail.

Existing experimental methods, such as those using a high-speed camera, particle image velocimetry (PIV), and planar laser-induced fluorescence (PLIF), encounter difficulties in obtaining information on the details inside the combustion zone [24–26]. Moreover, the complex combustor geometry further exacerbates the difficulties associated with experimental measurements. Notably, the computational fluid dynamics method can effectively quantify the turbulent flow field and flame propagation inside a combustion chamber. Chen et al. [27] studied combustion instability using Openform. Mansouri et al. [28,29] performed numerical simulations of flame characteristics using the Reynolds-averaged Navier–Stokes technique. Despite providing some promising results, their study was limited by coarse resolution in terms of the turbulent eddies. In this context [30,31], LES represents a highly effective tool for predicting turbulent flow and flame propagation characteristics and can reduce computational costs. In recent years, the corpus of studies on turbulent combustion using LES has grown.

In this study, the effects of primary and secondary holes on flame propagation and combustion instability were investigated using the LES and power spectral density (PSD) techniques. By analyzing the relationships among pressure oscillation, flame propagation, and unsteady flow fields, this study provides detailed insights into the potential mechanisms driving different combustor geometry combustion instability characteristics.

2. Materials and Numerical Methods

2.1. Numerical Model

In this study, the three-dimensional LES equations were employed as the governing equations using a commercial computational fluid dynamics software, ANSYS Fluent 2020. The dynamic Smagorinsky LES subgrid-scale model was used to process the instability characteristics in the presence of turbulent reactive flow. The governing equations, after being spatially and Favre-filtered [31,32], were formalized as follows:

$$\frac{\partial \bar{\rho}}{\partial t} + \frac{\partial (\bar{\rho} \tilde{u}_i)}{\partial x_j} = 0 \quad (1)$$

$$\frac{\partial (\bar{\rho} \tilde{u}_i)}{\partial t} + \frac{\partial (\bar{\rho} \tilde{u}_i \tilde{u}_j)}{\partial x_j} = \frac{\partial}{\partial x_j} (-\delta_{ij} \bar{p} + \tilde{\tau}_{ij} - \tau^{SGS}) \quad (2)$$

$$\frac{\partial}{\partial t} (\bar{\rho} \tilde{h} - \bar{p}) + \frac{\partial}{\partial x_j} (\bar{\rho} \tilde{h} \tilde{u}_j + h_j^{SGS}) = \frac{\partial}{\partial x_j} (-\tilde{q}_j + \tilde{\tau}_{ij} \tilde{u}_i - \sigma_j^{SGS}) \quad (3)$$

$$\frac{\partial}{\partial t} (\bar{\rho} \tilde{Y}_m) + \frac{\partial}{\partial x_j} [\bar{\rho} \tilde{Y}_m \tilde{u}_j - \bar{\rho} \tilde{Y}_m \tilde{V}_{j,m} + Y_{j,m}^{SGS} + \theta_{j,m}^{SGS}] = \tilde{\omega}_m \quad (4)$$

Equations (1)–(4) describe the conservation of mass, momentum, energy, and species conservation, respectively, after spatial and Favre filtering. The stress tensor τ_{ij} can be expressed as follows:

$$\tau_{ij} = \overline{u_i u_j} - \overline{u_i} \overline{u_j} \quad (5)$$

where μ denotes the molecular viscosity; and τ^{SGS} and V_t are the subgrid-scale stress tensor and viscosity, respectively.

$$\tau^{SGS} = -2\overline{\rho} v_t \left(\tilde{S}_{ij} - \frac{1}{3} \delta_{ij} \tilde{S}_{kk} \right) \quad (6)$$

$$v_t = (G\Delta)^2 \left(2\tilde{S}_{ij} \tilde{S}_{ij} \right)^{1/2} \quad (7)$$

where S_{ij} is the resolved strain rate tensor; and Δ and G are the filter width and kernel in the dynamic Smagorinsky–Lilly model, respectively. Note that the subgrid-scale total enthalpy and convective species flux are expressed according to the following equations:

$$h_j^{SGS} = -\overline{\rho} \frac{v_t}{pr_i} \cdot \frac{\partial \tilde{h}}{\partial x_j} \quad (8)$$

$$Y_{j,m}^{SGS} = -\overline{\rho} \frac{v_t}{Sc_t} \cdot \frac{\partial \tilde{Y}_m}{\partial x_j} \quad (9)$$

2.2. Reaction Model

In this study, the combustion model adopted the partially premixed equilibrium chemical reaction model. A 44-species and 78-reactions surrogate fuel RP-3 chemical kinetic mechanism [33–35] was employed in the simulation. The adopted flamelet-generated manifold (FGM) approach is based on the widely used and broadly acknowledged flamelet concept. The basis of the FGM approach is the generalized description of the flame front in a flame adaptation coordinate system. The FGM is an efficient and accurate modeling approach for premixed flames. Oijen applied the FGM to the modeling of turbulent flames using the LES flow solver [36].

The mixture fraction was formalized as follows:

$$Z = \frac{Y_i - Y_{i,ox}}{Y_{i,fuel} - Y_{i,ox}} \quad (10)$$

The subscript *ox* denotes the value at the oxidizer stream inlet, and the subscript *fuel* denotes the value at the fuel stream inlet. The Favre-filtered governing transport equation of Z is expressed as:

$$\frac{\partial}{\partial t} \left(\rho \tilde{Z} \right) + \nabla \cdot \left(\rho \tilde{u} \tilde{Z} \right) = \nabla \cdot \left(\frac{\mu_l + \mu_t}{\sigma_t} \nabla \tilde{Z} \right) \quad (11)$$

The normalized mass fraction (reaction progress variable C) of products is expressed as follows:

$$C = \frac{\sum_k \partial k (Y_k - Y_k^u)}{\sum_k \partial k (Y_k^{eq} - Y_k^u)} = \frac{Y_C}{Y_C^{eq}} \quad (12)$$

The subscript denotes the unburnt reactant, and Y_k denotes the k th species mass fraction. The transport equation of Y_C is solved as:

$$\overline{\rho} \frac{\partial}{\partial t} \left(\tilde{Y}_C \right) + \nabla \cdot \left(\overline{\rho} \tilde{u} \tilde{Y}_C \right) = \frac{\partial}{\partial x_i} \left(\overline{\rho} D_{eff} \frac{\partial \tilde{Y}_C}{\partial x_i} \right) + \overline{S_C} \quad (13)$$

2.3. Computational Details

A schematic of the combustor structure is shown in Figure 1. The computational domain was a 1/20-sector annular combustion chamber with a period-symmetric structure.

The inner radius of the combustor was 168 mm, the outer radius was 306 mm, and the axial length was 332 mm. The outer diameter of the swirler was 69 mm. The outer diameters of the primary and secondary holes were 16 and 9 mm, respectively. The swirler, primary holes, and secondary holes were 144, 229, and 261 mm in diameter from the inlet, respectively. The combustor included a triple swirler with swirl angles of 40° , 45° , and 45° . Air entered the combustion zone through the swirler, mixed with the fuel, and underwent reactions. The walls of the combustion chamber were cooled with the injection of air through the cooling film. Note that the axial and radial axes were the X and Y axes, respectively. According to different combustion chamber geometries, four cases were considered, as shown in Table 1. Case 1 included primary and secondary holes, Case 2 included only primary holes, Case 3 included only secondary holes, and Case 4 implied the absence of any holes.

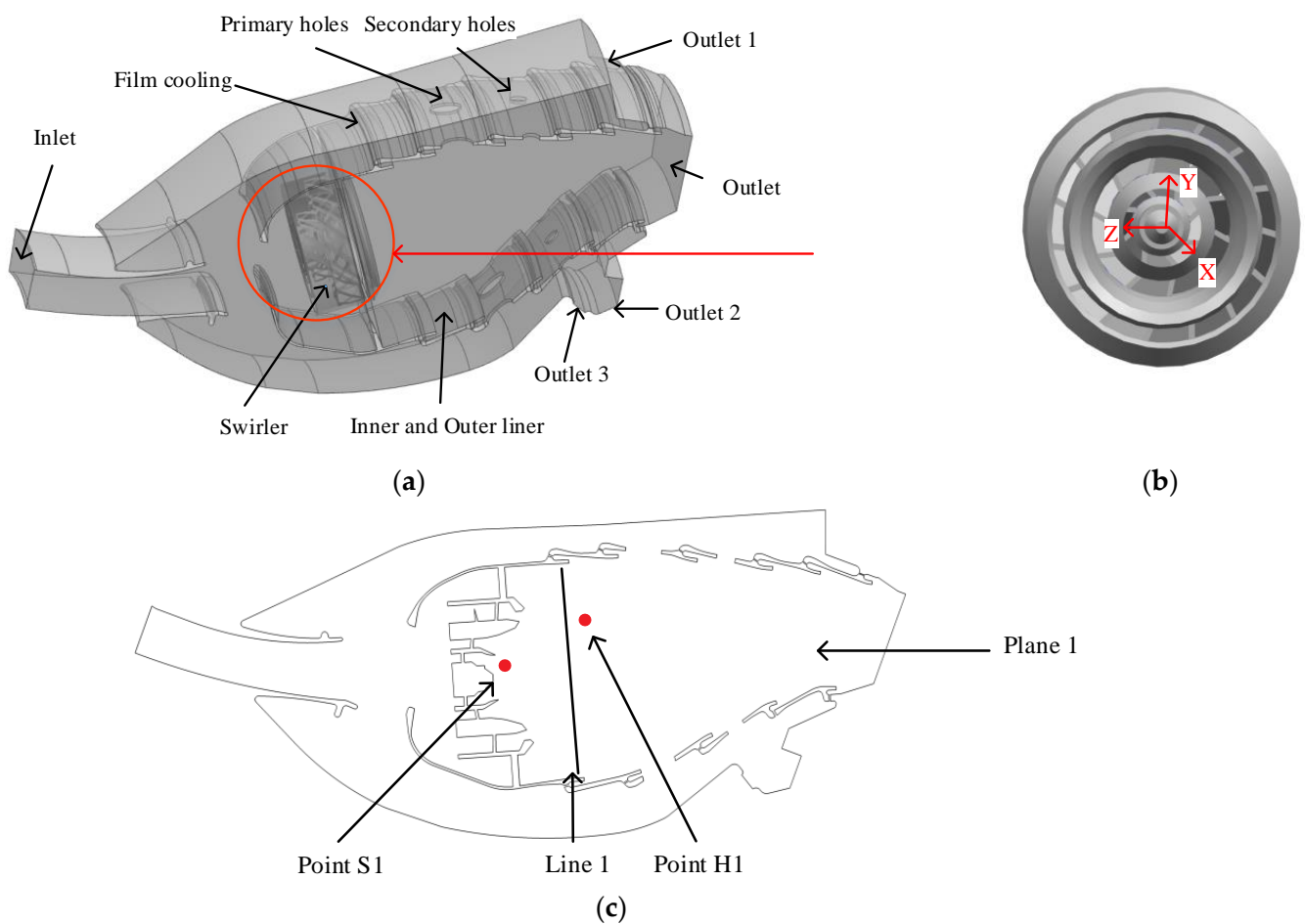


Figure 1. Three-dimensional view of combustion chamber: (a) combustion chamber; (b) swirler; (c) midplane.

Table 1. Different combustion chamber geometries.

Name	Primary Holes	Secondary Holes
Case 1	yes	yes
Case 2	yes	no
Case 3	no	yes
Case 4	no	no

Adaptive mesh refinement was applied to mesh the combustor model with a poly-hexacore, as shown in Figure 2. The grid dependency was evaluated at three grid levels

prior to the simulation. The moderate grid included 3,972,056 cells. The finer and coarser grids included 7,801,743 and 859,419 cells, respectively. Figure 2 shows a comparison between the pressure and temperature distribution distance for the three grids from the X coordinate, i.e., 25 mm (line 1).

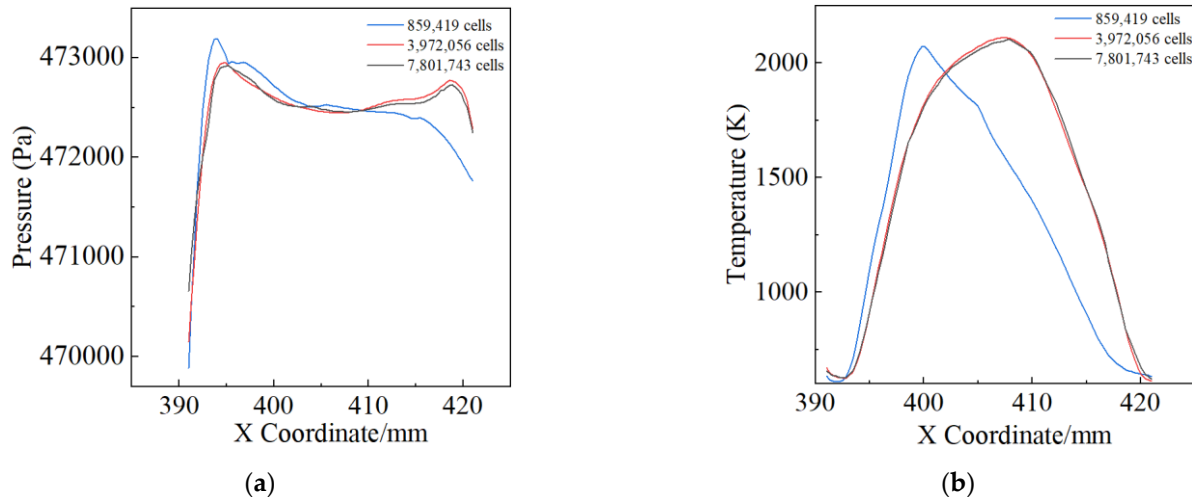


Figure 2. Grid sensitivity analyses: (a) pressure; (b) temperature.

The analysis revealed that the grid with 859,419 cells was exceedingly coarse, and the pressure and temperature distribution results of the fine grid were comparable to those of the moderate grid. Thus, the current selection of 3,972,056 cells was deemed to be sufficient. Figure 3 shows the grid of the combustor model, where the minimum orthogonal quality of meshing was >0.4 .

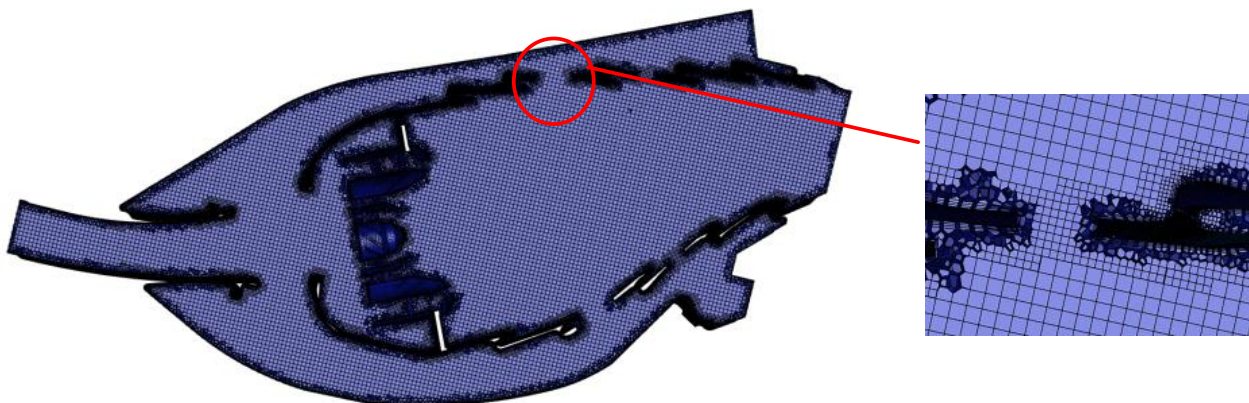


Figure 3. Grid distributions.

The kinetic energy spectra of H1 in the reaction region under the four cases are shown in Figure 4. A comparison with the $-5/3$ law showed that the simulation can reasonably predict the inertial behavior [37]. Moreover, Figure 4 demonstrates that the smallest resolution scale was in the inertial range of the turbulent kinetic energy spectra. Owing to this, it was reasonable to correct the LES method in this study to the turbulent motion in the reaction zone. Accordingly, we considered that the grid met the requirements of an LES in this study.

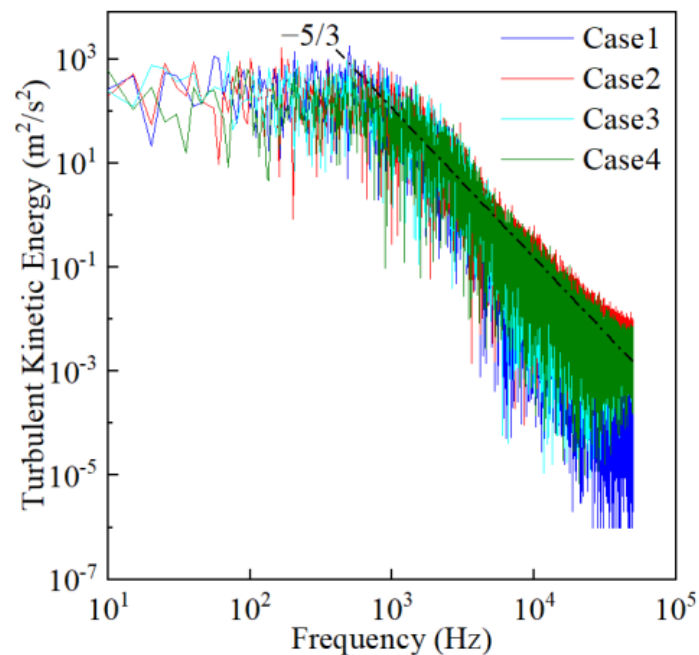


Figure 4. Kinetic energy spectra of H1 within the reaction zone for four cases.

In this study, the unsteady combustion of aviation kerosene and air was examined in various geometrical combustor models using the LES. The inlet pressure was set to 0.5 MPa. The inlet air and fuel temperatures were 600 and 300 K, respectively. The fuel and air inlet mass flow values were 7.667 and 550 g/s, respectively. Moreover, pressure–velocity coupling was achieved through the SIMPLE algorithm. The CPU processing time for each case was 210 h through parallel computation using 64 cores on the Beihang University supercomputer.

2.4. Model Evaluation

Figure 5 illustrates a schematic of the experimental setup. The experimental setup was composed of a charge-coupled device camera, frame grabber, computer, synchronizer, signal generator, laser optics, particle stroller, and high-pressure gas bottle. The construction and operation of the experimental device were performed in the combustion laboratory of Beihang University. The numerical simulation methods were previously evaluated [38,39]. Some transient axial velocity results were included in this study to confirm the accuracy of the numerical simulations.

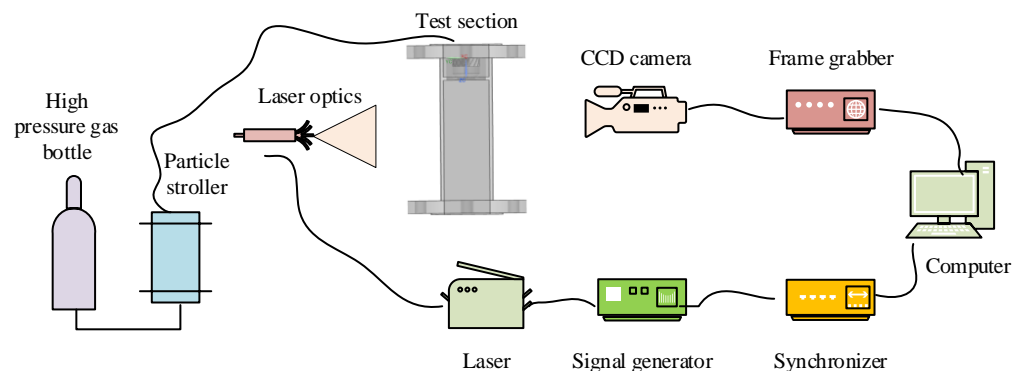


Figure 5. Schematic of the particle image velocimetry setup.

The average absolute relative deviation (AARD) between the simulated and experimental results was calculated to represent the error between the numerical results and the experimental results. The AARD values of the axial velocities at the four positions are shown in Table 2. The AARD values indicated that the errors between the experimental and numerical simulation results were small, and the relevance of the two was evident. Considering the empirical accuracy limitations, the numerical simulation results are considered acceptable.

Table 2. AARD of axial velocity.

Coordinate (mm)	35	40	60
AARD	4.57%	6.01%	12.04%

Figure 6 shows the comparative distribution of transient axial velocities from the experiments [38,39] and numerical simulations at various radial positions. The obtained velocity fields demonstrated good agreement with the experimental results at four specific locations, and the LES also accurately captured the drastic increase in the flow field. Moreover, the LES could better capture the central recirculation zone, accurately obtaining the peak of the axial velocity. Accordingly, we suggest that the numerical simulation results agree well with the experimental results. Thus, the numerical method used in this study is reliable.

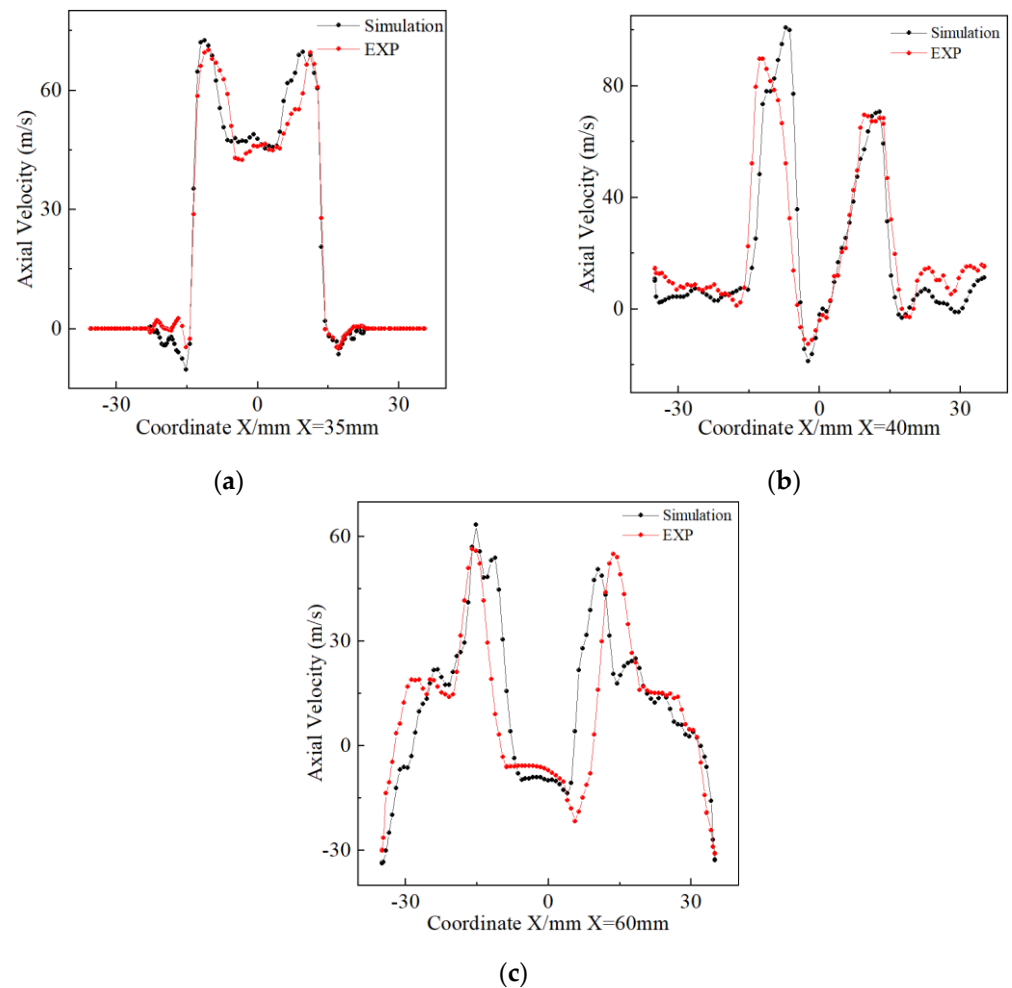


Figure 6. Comparisons between the numerical and experimental results: (a) $X = 35$ mm; (b) $X = 40$ mm; (c) $X = 60$ mm.

Figure 7 shows the velocity contour distribution obtained by comparing the experimental and simulation results. Figure 7 shows the movement of the high-speed airflow in the center recirculation zone and the high-speed airflow at the exit of the swirler. The shape of the center recirculation zone appears the same in the experimental and simulation results, and the peak velocity and size of the center recirculation zone are also the same. Thus, the reliability of the numerical simulation method was verified again by the experimental and simulation results.

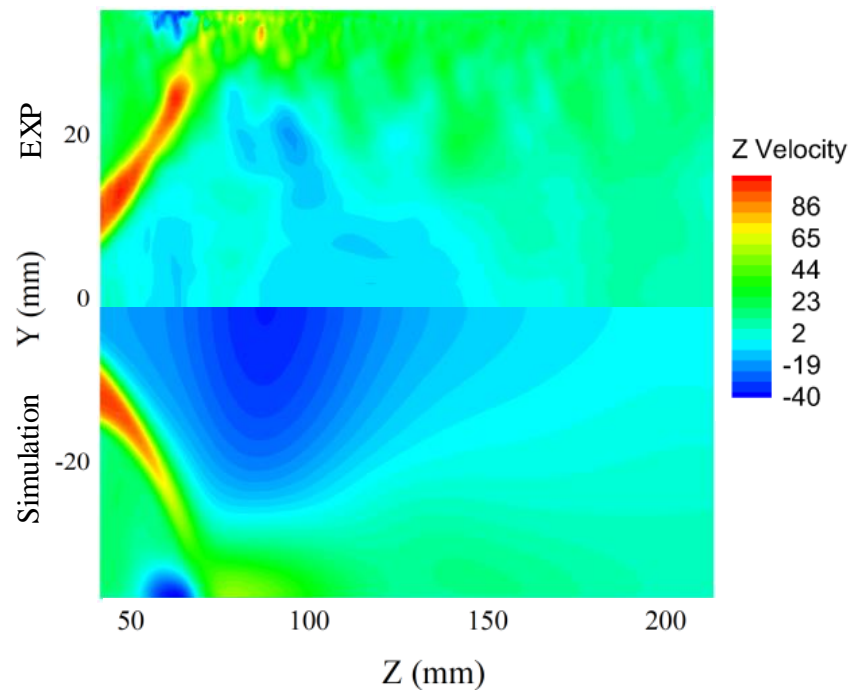


Figure 7. Velocity contour distribution in the midplane.

3. Results

3.1. Large-Eddy Simulation Analysis

Previous experimental studies have shown that the PVC is unstable in a combustion field [40]. However, their experimental observations have been limited to plane measurements, resulting in considerable limitations on their methodologies. Therefore, the LES method was used in this study to analyze the combustion instability patterns in both the stable and unstable states of the flames. The LES could provide the precise vortices generated in the combustion chamber, which were visualized through the instantaneous iso-surface and a vortex structure near the pilot-stage swirler. Figure 8 shows that with the pressure iso-surface, a large-scale structure was often identified in turbulent flows. It is the so-called precession vortex core, which was found in this combustor. Figure 8 illustrates four case snapshots to demonstrate the development of the PVC and branches. Owing to the intensification of flame fluctuation, the PVC rapidly spread out at the swirler exit and dissociated into small-scale vortex structures. This movement of the PVC caused unstable flow in the combustion chamber but enhanced the mixing level. Figure 8 also shows that the PVC markedly changed during periods of combustion instabilities for the combustor in Case 1. This was mainly owing to the enhanced mixing of the combustion chamber gases with the primary and secondary introduction of injected air. The precession of the PVC causes unstable periodic fluctuations in the flames, and the mixing of fresh reactant and burned products directly results in a strong reaction.

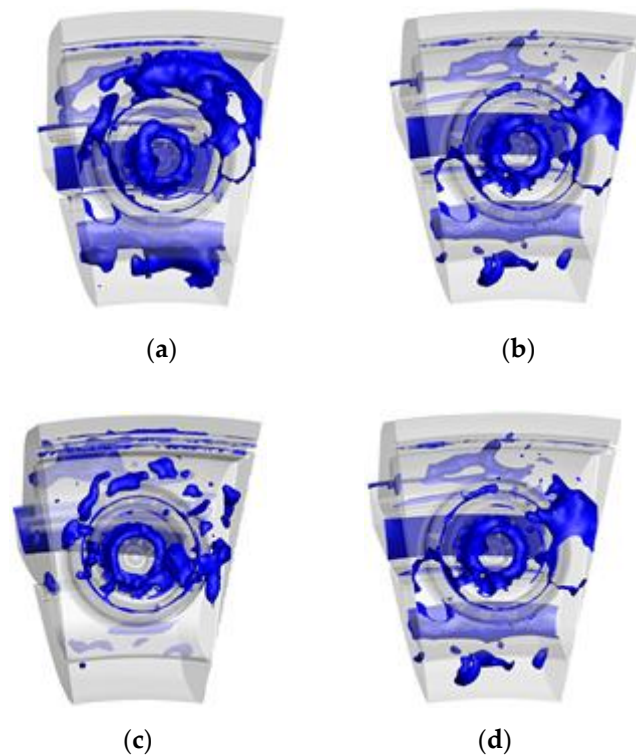


Figure 8. Three-dimensional structure of the precessing vortex core at $p = 0.4678$ MPa for four cases: (a) Case 1; (b) Case 2; (c) Case 3; (d) Case 4.

To elucidate the large-scale vortex in combustion dynamics in detail, the three-dimensional structure of the vortex breakdown bubble (VBB) was determined using instantaneous pressure (Figure 9). The VBB is the backflow region formed by the adverse pressure gradient resulting from the swirling motion. Owing to the periodic instability of the vortex shedding itself, it is coupled with the pressure fluctuations in the turbulent field during the interaction with the flame, causing visible combustion oscillations. The VBB can potentially represent a bubble around the centerline or a ring-shaped structure, which fundamentally depends on the nature of the inflow vortex. The unsteady behavior of the VBB can reflect the interaction of the flame and vortex within the combustor. Figure 9 shows that the range of the VBB in Case 1 was considerably wider than that in the other three cases. Moreover, the VBB interaction with flame propagation exacerbated the combustion instability in the turbulent field.

Figure 10 shows the instantaneous temperature snapshots along plane 1 for the four geometrical combustor models. Notably, four high-temperature areas were identified in the temperature fields. In all cases, flame stability was achieved by the interaction of the reversed hot products with the incoming reactants in the combustion process. The reaction zone was more compact, and the temperature distribution along plane 1 was less uniform in Case 1. This pattern was one of the key drivers behind the generation of combustion instability. During temperature pulsation, a distinct phenomenon of irregular temperature distribution in the downstream direction was identified, particularly in the vicinity of the primary and secondary holes. Moreover, the flame with high-temperature values was salient near the CRZ region in Case 1. The Kelvin–Helmholtz instability in the shear layer induced the instability in the CRZ. The contribution of temperature fluctuations and VBBs to unsteady combustion was anticipated to be high in Case 1. The disturbances in the flow field caused by the mixing of jet air from the primary and secondary holes with the air in the combustion chamber resulted in more pronounced temperature pulsations downstream of the combustion field. The interaction between the vortex structures and flame certainly caused some combustion instability. Moreover, the interaction of the jet air around the

primary and secondary holes with the small-scale eddies in the combustion field inevitably caused a certain degree of temperature pulsation, resulting in unstable combustion.

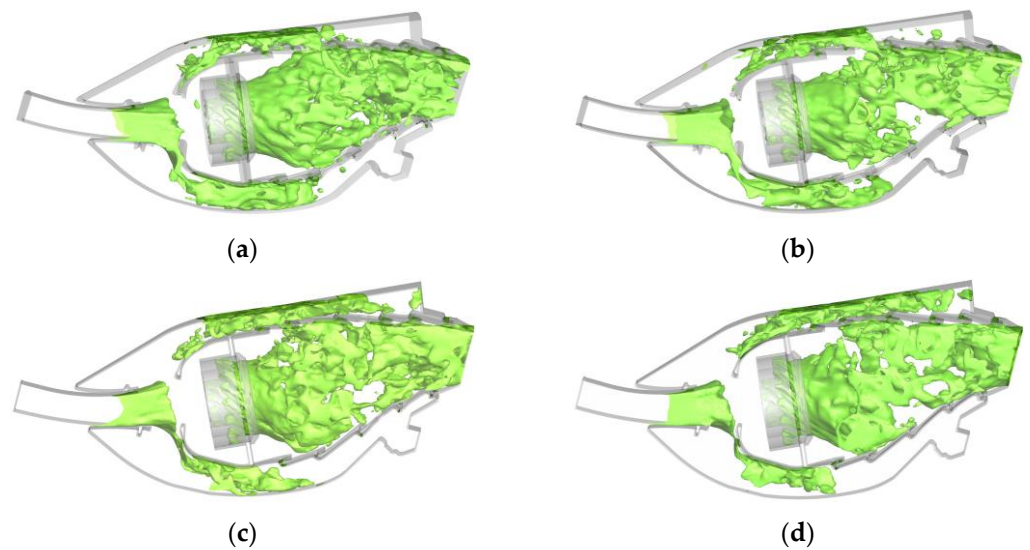


Figure 9. Three-dimensional structure of the vortex breakdown bubble for four cases: (a) Case 1; (b) Case 2; (c) Case 3; (d) Case 4.

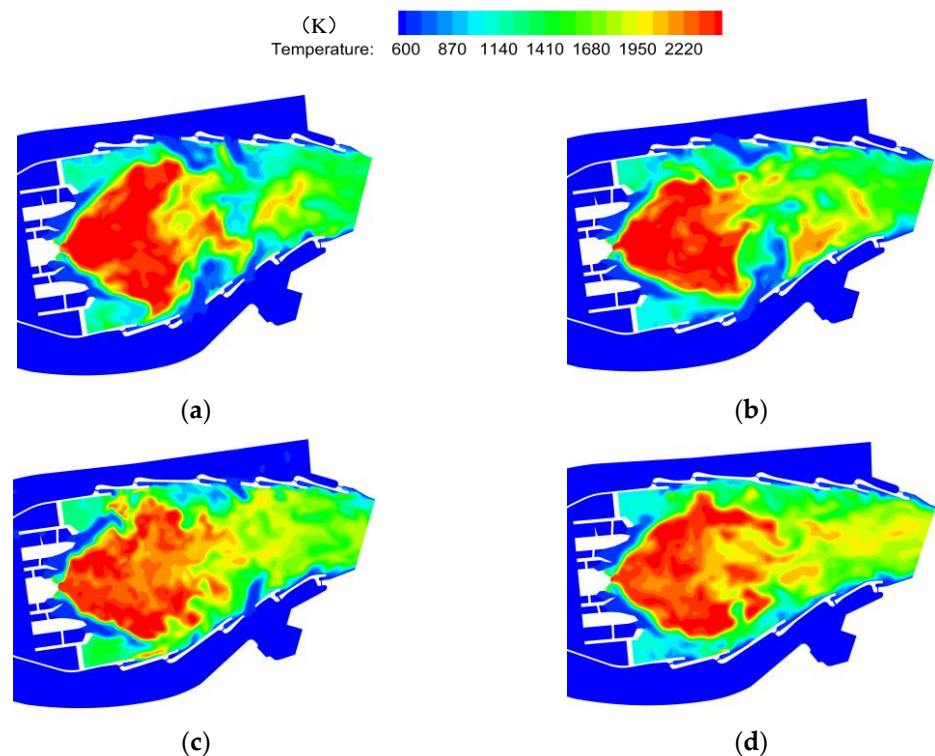


Figure 10. Instantaneous temperature distributions in the midplane at 0.2 s for four cases: (a) Case 1; (b) Case 2; (c) Case 3; (d) Case 4.

To evaluate this observation, we compared the computed variation of temperatures calculated for the four cases along line 1 (Figure 11). Given the different geometrical combustor models, a substantial change in the temperature pulsation was discerned. It was also clearly evident that the combustion became progressively more intense with increasing temperature fluctuations as the amount of air injected into the primary and secondary holes increased. Figure 11 also demonstrates that the temperature peaks were at 2462, 2453, 2455, and 2432 K, indicating that the temperature pulsation in the combustion zone was driven

by the injection of air through the primary and secondary holes, which, in turn, affected unsteady combustion.

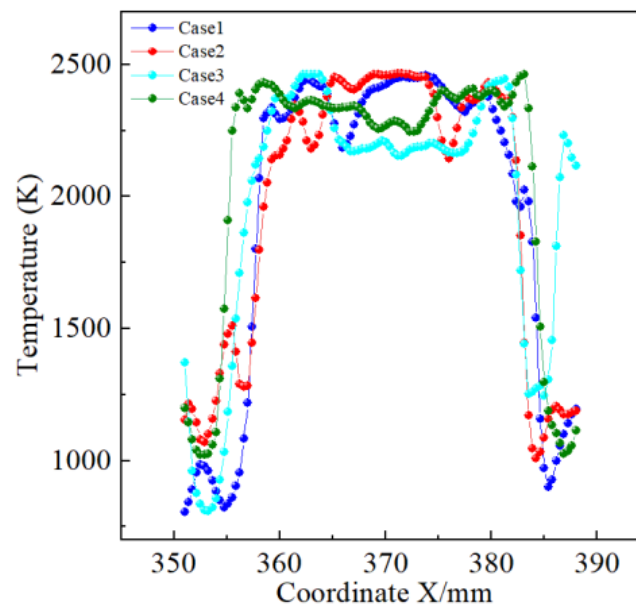


Figure 11. Axial velocity profiles for the four cases along line 1.

The time-evolution characteristics were further analyzed in detail to elucidate the impact of flame fluctuation on the unsteady combustion flow field. The change in flame state was well captured in the LES. The primary and secondary holes enhanced the mixing of fuel and air, strengthening combustion and shortening the flame length.

Notably, flame pulsation in Case 1 was represented by the OH distribution at specific times (Figure 12). The instantaneous mass fraction of the OH fields shown in Figure 12 indicates that the flame characteristics differed at various times. At $t = 0.01$ s, as fuel injection into the combustor was initiated, the flame also started developing and continuously provided thermal energy to the flow field as the VBB moved, thus increasing the rate of heat release for the combustor. At $t = 0.08$ s, the fuel was continuously injected into the combustor to create a maximum flame structure. At the downstream side of the flow field, air entered from the primary and secondary holes, and the disturbance of the flow field exacerbated the flame pulsation. The oscillation in combustion increased the combustion instability of the combustion chamber.

Moreover, the primary and secondary holes exacerbated the combustion instability characteristics. Excessive air convection triggered more heat loss. The combustion instability in the combustion chamber was also enhanced.

3.2. Power Spectral Density Analysis

Figure 13 indicates that the combustion instability characteristics were captured by analyzing pressure signals at points S1 and H1 in the swirler outlet and along the boundary layer of the recirculation zone (shown in Figure 1). This indicated that periodic pressure oscillations occurred in the combustion fields for the four cases. Figure 13a shows that the maximum pressure was 10.704 KPa in Case 1. At H1, the highest oscillation intensity was found in Case 1, with the peak value of 10.97 KPa at 0.14 s (Figure 13b). Figure 13 reveals that without primary and secondary hole structures, the pressure amplitude decreased, and the decreasing rate accelerated. Moreover, unsteady combustion increased. Therefore, the pressure oscillation amplitudes increased owing to the combustion instability related to the primary and secondary holes.

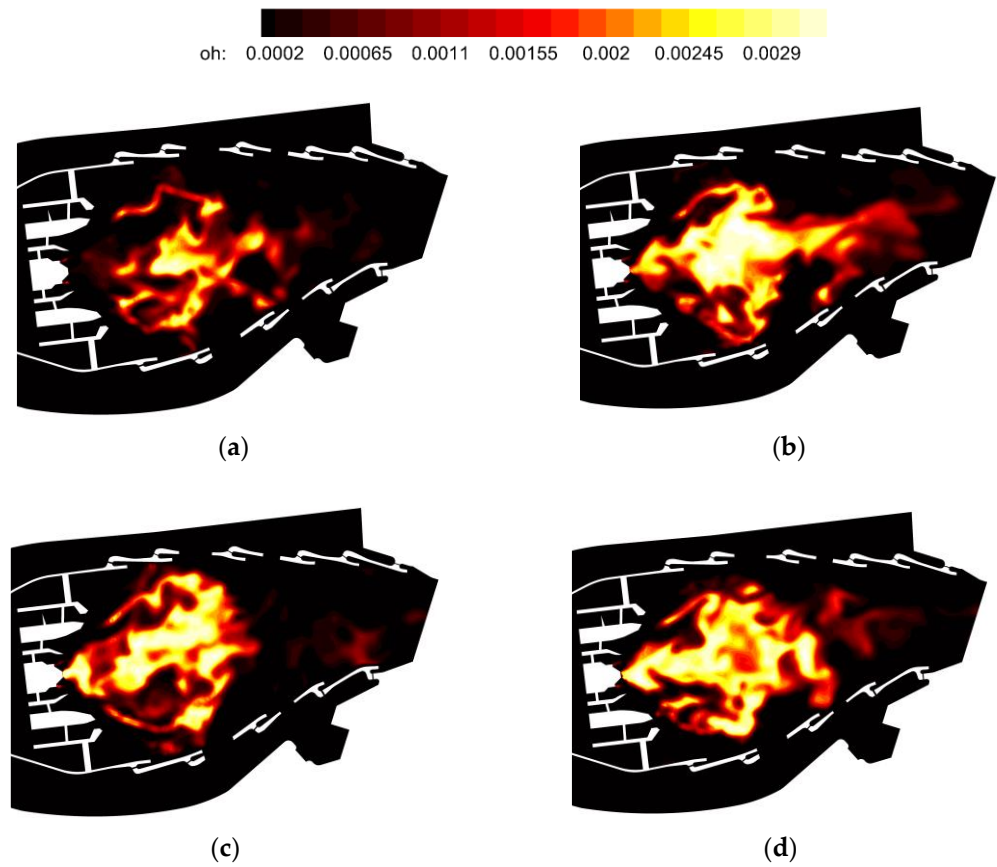


Figure 12. Instantaneous OH mass fraction in the midplane for Case 1: (a) $t = 0.01$ s; (b) $t = 0.08$ s; (c) $t = 0.16$ s; (d) $t = 0.2$ s.

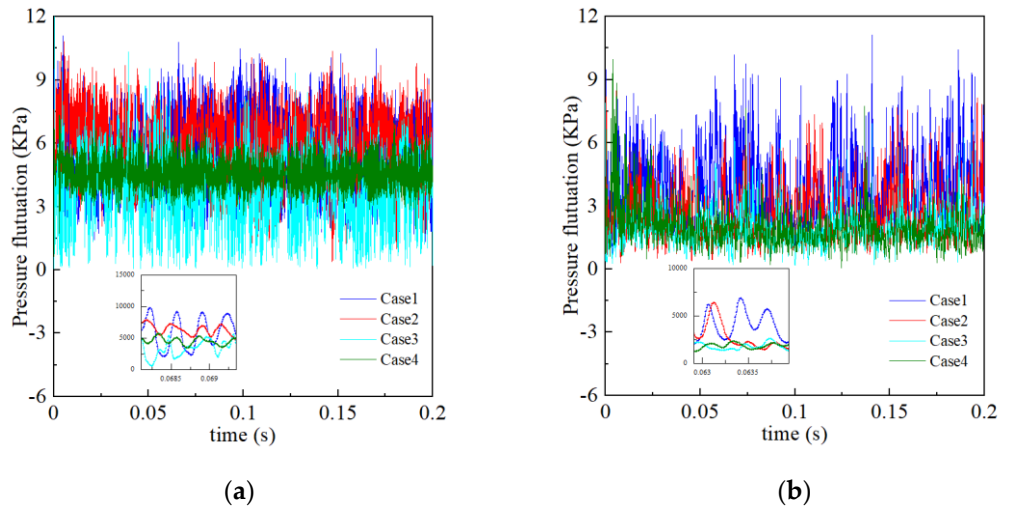


Figure 13. Pressure fluctuation at monitoring points: (a) S1; (b) H1.

Notably, the difference in the structures of the primary and secondary holes directly affected the heat release rate and, thus, the unsteady reaction flow characteristics. The heat release rate at monitoring point H1 for different cases is shown in Figure 14, which highlights that as the number of primary and secondary holes increased, the heat release rate at the monitoring point increased, and the variation accelerated. The amplitude in Case 1 reached a peak value of 8×10^{10} W at $t = 0.12$ s, whereas the amplitude in Case 4 reached a maximum value of 3.8×10^{10} W at $t = 0.1$ s. Unsteady combustion and flame pulsation were more intense in Case 1 than in the other cases. The structures of the primary

and secondary holes enhanced the flame pulsation in the combustion field and the heat release rate, resulting in increased unsteady combustion in the combustion chamber. This unsteady combustion was further intensified by pressure and flame pulsation, and the peak heat release fluctuation for Case 1 was larger than that for Case 4. Therefore, as the numbers of primary and secondary holes increased, the heat release rate increased.

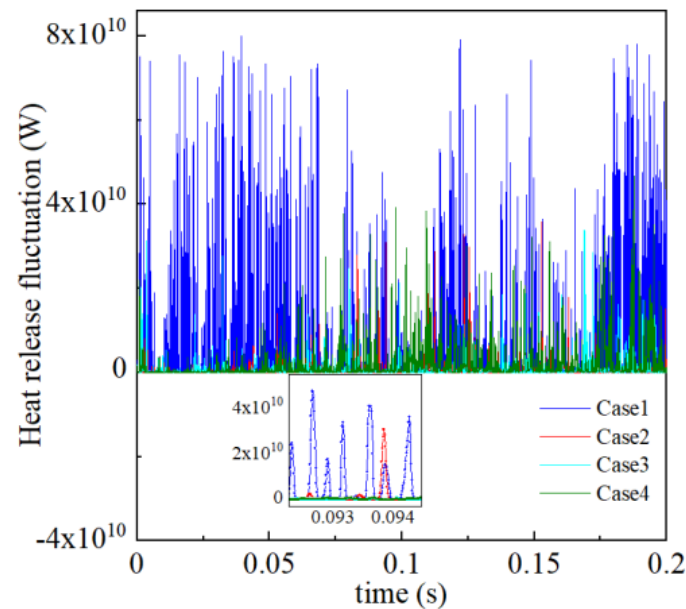


Figure 14. Heat release fluctuation in the four cases at point H1.

Point S1 was selected to monitor the pressure and perform fast Fourier transform analysis as well as PSD calculations using the data corresponding to the four cases. Figure 15a presents the influence of the primary and secondary holes on the dominant frequency and oscillation energy of the four cases at monitoring point S1. The four cases highlight that the dominant frequencies of the pressure fluctuations corresponded to high-frequency oscillations. Despite dominant frequency similarities, the four cases differed markedly in terms of the change in oscillation amplitude. The maximum value of the oscillation amplitude at point S1 was 5653 Pa^2 in Case 1, whereas the maximum value was only 1130 Pa^2 in Case 4. When the combustion chamber was equipped with both primary and secondary holes, the amplitude of the pressure fluctuation at the monitoring point gradually increased, the oscillation energy gradually increased, and the instability characteristics in the combustion field were also aggravated. With the addition of injected flow through the primary and secondary holes, the effect of flame combustion was enhanced, leading to the acceleration of flame propagation, thus increasing oscillation combustion in the combustion field. Meanwhile, the high oscillation amplitude produced significant instability characteristics. Therefore, as the numbers of primary and secondary holes increased, the pressure pulsation and oscillation energy increased.

Figure 15b shows the PSD of the pressure fluctuations at H1 on the boundary of the CRZ for the four cases. The dominant frequency at point H1 corresponds to the low-frequency oscillation induced by the Kelvin–Helmholtz effect, which, in turn, was affected by the primary and secondary holes. On the boundary of the CRZ, the Kelvin–Helmholtz instability was enhanced owing to the flow injected through the primary and secondary holes, resulting in greater oscillation energy at monitoring point H1. The frequency fluctuation range substantially differed between the four cases. The dominant frequencies in Cases 3 and 4 fluctuated in the range of 0–1000 Hz, whereas the dominant frequency in Case 1 with primary and secondary holes fluctuated from 0 to 4000 Hz. The maximum oscillation energy in Case 1 was five times more than that in Case 4, confirming that the combustor was affected by the injection flow through the primary and secondary holes.

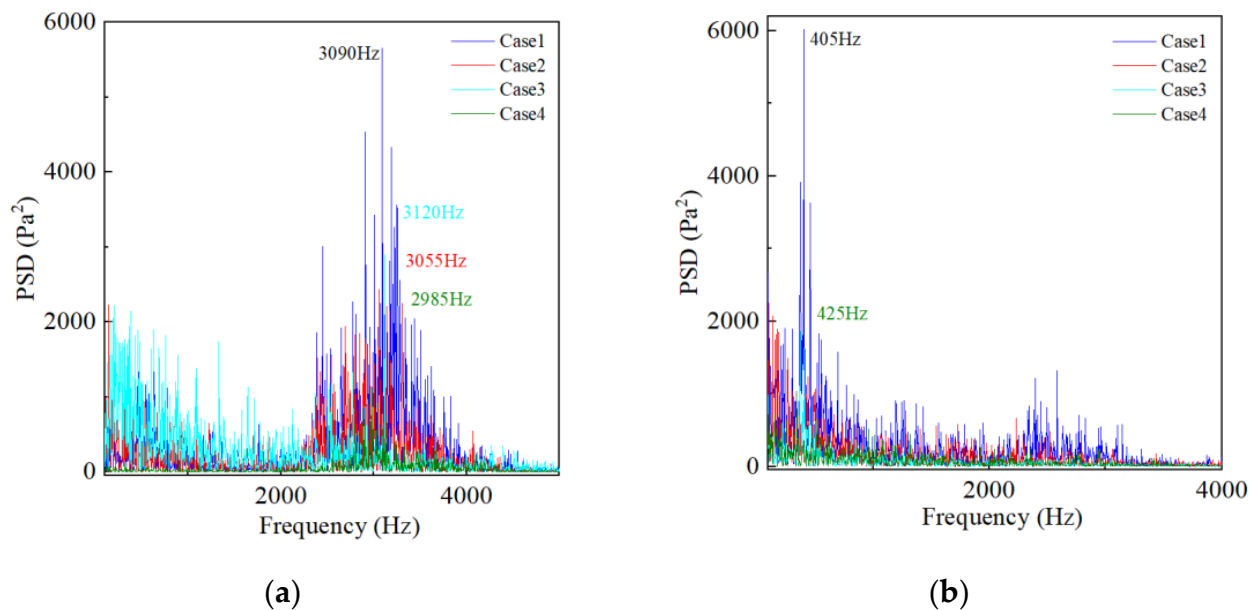


Figure 15. Power spectral density plots at monitoring points for four cases: (a) S1; (b) H1.

4. Conclusions

In this study, the effects of primary and secondary holes on flame fluctuation and pressure oscillation combustion instability in complex triple swirler stage combustion chambers were investigated using the LES and PSD methods.

The results corresponding to the instantaneous temperature and flame field were associated with unsteady combustion characteristics, namely large-scale vortex structures and the Kelvin–Helmholtz instability, which enhanced unsteady combustion. In the combustion chamber reaction flow field, the large-scale vortex structure and Kelvin–Helmholtz instability in the shear layer region were found to be affected by the primary and secondary holes. Among the influencing factors, the injection flow through the primary and secondary holes played a significant role in the flame and temperature fluctuations, whereas flame fluctuation influenced the heat release rate of the combustion field.

The variations in energy amplitudes and pressure oscillations in the presence of primary and secondary holes were quantitatively analyzed. The influence of the oscillating amplitude was found to be maximized in the presence of the primary and secondary holes, leading to combustion instability in the combustion chamber. With the injection flow through the primary and secondary holes, the oscillating energy increased, and the frequency fluctuation range correspondingly widened. The maximum value of the oscillation amplitude at point S1 was 5653 Pa^2 with primary and secondary holes. Moreover, low-frequency oscillations dominated by the Kelvin–Helmholtz model in the central recirculation region also affected the combustion instability process.

Notably, this study was limited to investigations of combustion instability based on the influence of large-scale vortex structures, flame propagation, and pressure oscillation. Although unsteady characteristics were relatively accurately captured, thermoacoustic oscillation in the combustion chamber has yet to be evaluated in detail. To comprehensively analyze dynamic combustion mechanisms, future studies can use commercial software to investigate the thermoacoustic combustion instability characteristics in combustion chambers.

Author Contributions: Conceptualization, methodology, software, validation, formal analysis, investigation, resources, data curation, writing—original draft preparation, writing—review and editing, visualization, N.M.; project administration, supervision, funding acquisition, F.L. All authors have read and agreed to the published version of the manuscript.

Funding: This research was funded by the National Science and Technology Major Project (J2019-III-0002-0045 and 2017-III-0006-0031).

Institutional Review Board Statement: Not applicable.

Informed Consent Statement: Not applicable.

Data Availability Statement: Not applicable.

Conflicts of Interest: The authors declare no conflict of interest.

References

1. Joo, S.; Kwak, S.; Lee, J.; Yoon, Y. Thermoacoustic Instability and Flame Transfer Function in a Lean Direct Injection Model Gas Turbine Combustor. *Aerosp. Sci. Technol.* **2021**, *116*, 106872. [[CrossRef](#)]
2. Khani Moghanaki, S.; Kazempour Liasi, H.; Mohammadi, H.; Nasrollahnejad, F. Effects of Secondary Combustion in a Gas Turbine on the Microstructural Evolution, Mechanical Properties, and Failure Mechanism of the Blades. *Eng. Fail. Anal.* **2022**, *139*, 106439. [[CrossRef](#)]
3. Yang, Y.; Liu, A.; Wang, X.; Xi, L.; Zeng, W. Influence of Structure on the Combustion Characteristics of a Small Aero-Gas Turbine Engine Combustor. *Fuel* **2022**, *321*, 124018. [[CrossRef](#)]
4. Tongroon, M.; Chuepeng, S. Adjacent Combustion Heat Release and Emissions over Various Load Ranges in a Premixed Direct Injection Diesel Engine: A Comparison between Gasoline and Ethanol Port Injection. *Energy* **2022**, *243*, 122719. [[CrossRef](#)]
5. Xia, Y.; Hashimoto, N.; Fujita, O. Turbulent Flame Propagation Mechanism of Polymethylmethacrylate Particle Cloud–Ammonia Co-Combustion. *Combust. Flame* **2022**, *241*, 112077. [[CrossRef](#)]
6. Wang, T.; Wang, Z.; Tan, J.; Sun, M.; Cai, Z.; Liu, Y. Combustion Characteristics of a Confined Turbulent Jet Flame. *Fuel* **2022**, *323*, 124228. [[CrossRef](#)]
7. Neumann, N.; Asli, M.; Garan, N.; Peitsch, D.; Stathopoulos, P. A Fast Approach for Unsteady Compressor Performance Simulation under Boundary Condition Caused by Pressure Gain Combustion. *Appl. Therm. Eng.* **2021**, *196*, 117223. [[CrossRef](#)]
8. Wan, J.; Zhao, H. Blow-off Mechanism of a Holder-Stabilized Laminar Premixed Flame in a Preheated Mesoscale Combustor. *Combust. Flame* **2020**, *220*, 358–367. [[CrossRef](#)]
9. Kim, G.T.; Park, J.; Chung, S.H.; Yoo, C.S. Effects of Non-Thermal Plasma on Turbulent Premixed Flames of Ammonia/Air in a Swirl Combustor. *Fuel* **2022**, *323*, 124227. [[CrossRef](#)]
10. Somarathne, K.D.K.A.; Okafor, E.C.; Hayakawa, A.; Kudo, T.; Kurata, O.; Iki, N.; Kobayashi, H. Emission Characteristics of Turbulent Non-Premixed Ammonia/Air and Methane/Air Swirl Flames through a Rich-Lean Combustor under Various Wall Thermal Boundary Conditions at High Pressure. *Combust. Flame* **2019**, *210*, 247–261. [[CrossRef](#)]
11. Sadatakhavi, S.M.R.; Tabejamaat, S.; EiddiAttarZade, M.; Kankashvar, B.; Nozari, M.R. Numerical and Experimental Study of the Effects of Fuel Injection and Equivalence Ratio in a Can Micro-Combustor at Atmospheric Condition. *Energy* **2021**, *225*, 120166. [[CrossRef](#)]
12. Ren, S.; Yang, H.; Jiang, L.; Zhao, D.; Wang, X. Combustion Modes and Driving Mechanisms of Pressure Fluctuation in a Novel Vortex-Tube Combustor with Quasi-Steady and Stratified Properties. *Exp. Therm. Fluid Sci.* **2020**, *117*, 110134. [[CrossRef](#)]
13. Palies, P.; Durox, D.; Schuller, T.; Candel, S. The Combined Dynamics of Swirler and Turbulent Premixed Swirling Flames. *Combust. Flame* **2010**, *157*, 1698–1717. [[CrossRef](#)]
14. Ozgunoglu, M.; Gungor, A.G. Large Eddy Simulation of Turbulence-Combustion Interactions in a Stagnation Point Reverse Flow Combustor. *Fuel* **2019**, *257*, 115988. [[CrossRef](#)]
15. Huang, D.; Xu, J.; Chen, R.; Meng, H. Large Eddy Simulations of Turbulent Combustion of Kerosene-Air in a Dual Swirl Gas Turbine Model Combustor at High Pressures. *Fuel* **2020**, *282*, 118820. [[CrossRef](#)]
16. Guo, K.; Ren, Y.; Chen, P.; Lin, W.; Tong, Y.; Nie, W. Analysis of Spontaneous Longitudinal Combustion Instability in an O₂/CH₄ Single-Injector Rocket Combustor. *Aerosp. Sci. Technol.* **2021**, *119*, 107209. [[CrossRef](#)]
17. Zeng, Z.; Ren, J.; Liu, X.; Xu, Z. The Unsteady Turbulence Flow of Cold and Combustion Case in Different Trapped Vortex Combustor. *Appl. Therm. Eng.* **2015**, *90*, 722–732. [[CrossRef](#)]
18. Wu, Y.; Carlsson, C.; Szasz, R.; Peng, L.; Fuchs, L.; Bai, X.S. Effect of Geometrical Contraction on Vortex Breakdown of Swirling Turbulent Flow in a Model Combustor. *Fuel* **2016**, *170*, 210–225. [[CrossRef](#)]
19. Stöhr, M.; Boxx, I.; Carter, C.D.; Meier, W. Experimental Study of Vortex-Flame Interaction in a Gas Turbine Model Combustor. *Combust. Flame* **2012**, *159*, 2636–2649. [[CrossRef](#)]
20. Salvador, F.J.; Carreres, M.; García-Tíscar, J.; Belmar-Gil, M. Modal Decomposition of the Unsteady Non-Reactive Flow Field in a Swirl-Stabilized Combustor Operated by a Lean Premixed Injection System. *Aerosp. Sci. Technol.* **2021**, *112*, 106622. [[CrossRef](#)]
21. Zhang, B.; Shahsavari, M.; Rao, Z.; Yang, S.; Wang, B. Contributions of Hydrodynamic Features of a Swirling Flow to Thermoacoustic Instabilities in a Lean Premixed Swirl Stabilized Combustor. *Phys. Fluids* **2019**, *31*, 075106. [[CrossRef](#)]
22. Nam, J.; Yoh, J.J. A Numerical Investigation of the Effects of Hydrogen Addition on Combustion Instability inside a Partially-Premixed Swirl Combustor. *Appl. Therm. Eng.* **2020**, *176*, 115478. [[CrossRef](#)]
23. Song, Y.; Li, J.; Yang, L. Effect of Flame Motion on Longitudinal Combustion Instabilities. *Aerosp. Sci. Technol.* **2022**, *122*, 107427. [[CrossRef](#)]

24. Wang, L.; Jiang, Y.; Qiu, R. Experimental Study of Combustion Inhibition by Trimethyl Phosphate in Turbulent Premixed Methane/Air Flames Using OH-PLIF. *Fuel* **2021**, *294*, 120324. [[CrossRef](#)]
25. Zhang, B.; Luan, B.; Dong, J.; He, J.; Chen, W. Simultaneous Deflection Tomography and PIV Measurements of Non-Premixed Combustion. *Opt. Lasers Eng.* **2020**, *127*, 105944. [[CrossRef](#)]
26. Johe, P.; Zentgraf, F.; Greifenstein, M.; Steinhausen, M.; Hasse, C.; Dreizler, A. Characterization of Flow Field and Combustion Dynamics in a Novel Pressurized Side-Wall Quenching Burner Using High-Speed PIV/OH-PLIF Measurements. *Int. J. Heat Fluid Flow* **2022**, *94*, 108921. [[CrossRef](#)]
27. Chen, Z.X.; Langella, I.; Swaminathan, N.; Stöhr, M.; Meier, W.; Kolla, H. Large Eddy Simulation of a Dual Swirl Gas Turbine Combustor: Flame/Flow Structures and Stabilisation under Thermoacoustically Stable and Unstable Conditions. *Combust. Flame* **2019**, *203*, 279–300. [[CrossRef](#)]
28. Broatch, A.; Carreres, M.; García-Tíscar, J.; Belmar-Gil, M. Spectral Analysis and Modelling of the Spray Liquid Injection in a Lean Direct Injection (LDI) Gas Turbine Combustor through Eulerian-Lagrangian Large Eddy Simulations. *Aerosp. Sci. Technol.* **2021**, *118*, 106992. [[CrossRef](#)]
29. Mansouri, Z.; Aouissi, M.; Boushaki, T. Numerical Computations of Premixed Propane Flame in a Swirl-Stabilized Burner: Effects of Hydrogen Enrichment, Swirl Number and Equivalence Ratio on Flame Characteristics. *Int. J. Hydrog. Energy* **2016**, *41*, 9664–9678. [[CrossRef](#)]
30. Wang, P.; Fröhlich, J.; Maas, U.; He, Z.; Wang, C. A Detailed Comparison of Two Sub-Grid Scale Combustion Models via Large Eddy Simulation of the PRECCINSTA Gas Turbine Model Combustor. *Combust. Flame* **2016**, *164*, 329–345. [[CrossRef](#)]
31. Zhang, M.; Liang, A. Large-Eddy Simulation and Linear Acoustic Modeling of Entropy Mode Oscillations in a Model Combustor with Coolant Injection. *Chin. J. Aeronaut.* **2018**, *31*, 1691–1702. [[CrossRef](#)]
32. Qi, H.; Li, X.; Yu, C. Subgrid-Scale Model Based on the Vorticity Gradient Tensor for Rotating Turbulent Flows. *Acta Mech. Sin. Xuebao* **2020**, *36*, 692–700. [[CrossRef](#)]
33. Liu, J.; Hu, E.; Zeng, W.; Zheng, W. A New Surrogate Fuel for Emulating the Physical and Chemical Properties of RP-3 Kerosene. *Fuel* **2020**, *259*, 116210. [[CrossRef](#)]
34. Wei, S.; Sun, L.; Wu, L.; Yu, Z.; Zhang, Z. Study of Combustion Characteristics of Diesel, Kerosene (RP-3) and Kerosene-Ethanol Blends in a Compression Ignition Engine. *Fuel* **2022**, *317*, 123468. [[CrossRef](#)]
35. Zhang, C.; Li, B.; Rao, F.; Li, P.; Li, X. A Shock Tube Study of the Autoignition Characteristics of RP-3 Jet Fuel. *Proc. Combust. Inst.* **2015**, *35*, 3151–3158. [[CrossRef](#)]
36. Van Oijen, J.A.; Donini, A.; Bastiaans, R.J.M.; ten Thije Boonkamp, J.H.M.; de Goey, L.P.H. State-of-the-Art in Premixed Combustion Modeling Using Flamelet Generated Manifolds. *Prog. Energy Combust. Sci.* **2016**, *57*, 30–74. [[CrossRef](#)]
37. Meneveau, C.; Lund, T.S.; Cabot, W.H. A Lagrangian Dynamic Subgrid-Scale Model of Turbulence. *J. Fluid Mech.* **1996**, *319*, 353–385. [[CrossRef](#)]
38. Meng, N.; Li, F. Large Eddy Simulations of Unsteady Non-Reaction Flow Characteristics Using Different Geometrical Combustor Models. *Aerosp. Sci. Technol.* **2022**, *126*, 107638. [[CrossRef](#)]
39. Meng, N.; Li, F. Large-Eddy Simulation of Unstable Non-Reactive Flow in a Swirler Combustor. *Phys. Fluids* **2022**, *34*, 114107. [[CrossRef](#)]
40. Bhattacharya, C.; De, S.; Mukhopadhyay, A.; Sen, S.; Ray, A. Detection and Classification of Lean Blow-out and Thermoacoustic Instability in Turbulent Combustors. *Appl. Therm. Eng.* **2020**, *180*, 115808. [[CrossRef](#)]

Disclaimer/Publisher’s Note: The statements, opinions and data contained in all publications are solely those of the individual author(s) and contributor(s) and not of MDPI and/or the editor(s). MDPI and/or the editor(s) disclaim responsibility for any injury to people or property resulting from any ideas, methods, instructions or products referred to in the content.